



## Investigating the Turbulent Flow around Semi-Circular Cylinder

Tahseen Ali Jabbar<sup>1</sup>, Rafi Mohammed Qasim<sup>2</sup>, Safaa Hameed Faisal<sup>1,\*</sup>, Bassam Abdullah Mohammed<sup>1</sup>

<sup>1</sup> Department of Thermal Mechanical Engineering, Basra Engineering Technical College, Southern Technical University, Basra, Iraq

<sup>2</sup> Department of Fuel and Energy Engineering, Basra Engineering Technical College, Southern Technical University, Basra, Iraq

### ARTICLE INFO

#### Article history:

Received 14 September 2023

Received in revised form 29 November 2023

Accepted 16 December 2023

Available online 31 December 2023

#### Keywords:

Turbulent flow; semi-circular cylinder;  
drag coefficient; lift coefficient; skin  
friction

### ABSTRACT

The Spalart-Allmaras turbulence model is used to study the flow patterns around a semi-circular cylinder surrounded by water in two dimensions with various angles of strike owing to rotating the cylinder by an angle. The rotation angle ranges from zero to 360° and the ANSYS Fluent software is employed to implement the required simulation. The Spalart-Allmaras turbulence model is used to determine the flow velocity vector, velocity contours, and pressure contours. Moreover, this turbulent model is used to calculate three different non-dimensional parameters, the drag coefficient, lift coefficient, and skin friction factors. Two different Reynolds numbers (Re) are adopted in the calculation of the three non-dimensional parameters with various values for the angle of the cylinder rotation. Here, the semi-circular cylinder is considered stationary but it is placed in a water domain in various positions. Due to the scarcity in information about using the Spalart-Allmaras turbulence model as compared with other models, which are widely used to investigate the flow around the cylinder, three turbulent models are employed to verify the results obtained by the Spalart-Allmaras model, these models are  $k - \epsilon$  (standard),  $k - \epsilon$  (RNG), and  $k - \epsilon$  (Realizable). Results show an excellent agreement between the four turbulent models compared, where there is no significant variation in the obtained results, all results are very similar.

## 1. Introduction

The flow around a body or an obstacle represents a challenge owing to the interaction between fluid and solid. The interest in this subject rises from the change in the flow field around a solid body, causing many changes in the pressure, flow velocity, streamlines, or any hydraulic parameters, which dominate this subject. This subject have a wide variety of engineering requests such as design of electronic items like transistors for best cooling, bridge pier design, extended surface design, and more. The flow around a cylinder body has been investigated for many decades, while the flow around a semi-circular body has been less often investigated than the cylinder body.

A review of some previous works related to flow around a cylinder and semi-circular cylinder is provided. Lysenko *et al.*, [1] numerically investigated the turbulent flow over a semi-circular cylinder

\* Corresponding author.

E-mail address: [s\\_hfaisal100@stu.edu.iq](mailto:s_hfaisal100@stu.edu.iq)

<https://doi.org/10.37934/arfmts.112.2.191213>

utilizing large eddy model, to achieve the simulation, OpenFOAM CFD is used to perform this purpose. In this numerical investigation a Re equal to 50000 based on the diameter and zero impact angle is adopted. Isaev *et al.*, [2] investigated numerically and experimentally the turbulent flow of air around semi-circular cylinder. The numerical investigation is done in two dimensions at Re equal to 50000 and zero angle of attack. The unsteady Reynolds Average Navier Stokes method (URANS) with different turbulent models is used. In addition, different structure grids and different approximation methods are used in this numerical investigation. The wind tunnel tests are used to validate the turbulent flow in two dimensions. Yamagata *et al.*, [3] conducted an experiment work in uniform flow to investigate the Aeolian tone from a semi-circular cylinder, considering different attack angles. They found the Aeolian tone sound spectrum at the peak of the semi-circular cylinder is smaller than Aeolian tone sound spectrum at the peak of the circular cylinder. Wornom *et al.*, [4] performed a computational analysis for the flow field around a circular cylinder. Here, the hydraulic regime is considered subcritical with the Reynolds number up to  $2 \times 10^5$  adopting a variational multiscale Large Eddy Simulation method. Tsutsui [5] investigated the applied wind force on the cylindrical structure with a low aspect ratio; the cylinder is placed in a turbulent boundary layer. Two different cylinder diameters are used while Reynolds numbers depended on the diameter, which varied from  $1.1 \times 10^4$  and  $1.1 \times 10^5$ . In addition, the thickness of the turbulent boundary layer at the position of the cylindrical structure varied from 26 mm-120 mm. The range of the aspect ratio varied from 0.125-1. Flow visualizations are performed depending on the surface oil-flow pattern method. Zhang *et al.*, [6] studied the flow pattern around a cylinder with a circular section in the critical regime by using a compressible wall-resolved Large Eddy Simulation (LES) for the first time. It is found that the results have good agreement with the previous experimental and incompressible LES data. Yagmur *et al.*, [7] did a numerical study to reveal the flow characteristics around a semi-circular cylinder; a computational fluid dynamic is used with Reynolds number equal to 3.2. The flow characteristics such as velocity field, streamline patterns, vorticity, Reynolds stress correlations, turbulent kinetic energy, drag and pressure coefficients have been studied. Reynolds averaged Navier-Stokes, Detached Eddy Simulation and Large Eddy Simulations referred to the turbulent model, which are adopted in the analysis of fluid-structure interaction. Barratt *et al.*, [8] studied experimentally the impinging of a round jet on a long cylinder that has a circular section, the round jet is considered fully turbulent. Here,  $Re=20000$  is based on the jet diameter. The study dealt with the kinematics of the boundary layer transmission that happens and produces a second thermal peak on the cylinder surface downstream of the primary thermal peak near the stagnation point when placed inside the jet's potential core. The spectral analysis is done for the data of shear stress at the wall and time-resolved of velocity inside both turbulent and laminar boundary layers. Pereira *et al.*, [9] examined the flow field around a cylinder that has a circular section at  $Re = 140000$  by using RANS (Reynolds-Averaged Navier–Stokes equations) and SRS (Scale-Resolving Simulation). The work concentrated on three objectives; (i) to estimate the aptitude of notable RAMS and SRS models in order to simulate the flow regime correctly, (ii) comparison between the predictions of the chosen methods and the available measurements from experimental, (iii) inspect the key modeling of the flow parameters that participate to the observed results. Salaheldin *et al.*, [10] investigated the turbulent flow by adopting a numerical computation three-dimensions around a vertical pier, which has a circular cross section. Different turbulent models are used; also, the obtained results are compared with many experimental available data. In spite of noticeable defects of the k- $\epsilon$  model in the solution of the three-dimension open channel and geophysical flows, many variants of this turbulent model are found to work successfully in reproducing the profile of the measured velocity. Also, a contrast is found between the model results with measured bed shear stress. Behrouzi *et al.*, [11] performed numerical computations around single pier and twin bridge piers by adopting fluent

model in order to simulate the turbulent kinetic energy and flow velocity. The pier and piers have a circular cross section. For both twin piers and single pier, the flow velocity components, velocity contours, and streamlines are investigated. Mammari and Soudani [12] studied numerically the flow around a cylinder in a channel with a fixed bed. CFD code is employed to analyze the field of flow and kinetic energy around the cylinder. The turbulent model used in this study is the standard k- $\epsilon$ . The predicted kinetic energy and velocity are compared with measured data. Sowoud *et al.*, [13] studied numerically the turbulent flow pattern over a circular cylinder in subcritical regimes, the cylinder is considered smooth and uniform. Also, the variation effect of the Reynolds number on the flow characteristics is studied. The standard k- $\epsilon$  is employed to describe the turbulent model. The investigation addresses the following: velocity components, pressure contours, pressure coefficient, and drag coefficient. The numerical computation is done in two dimensions by employing ANSYS Software. Catalano *et al.*, [14] carried out a large eddy simulation of the flow around a circular cylinder at high Reynolds numbers.

In this work, the computational fluid dynamic is implemented by utilizing ANSYS Fluent software in two dimensions flow field. The investigation is divided into three parts and these parts are:

- i. Examine the velocity vector, velocity contour, and pressure contour to realize the flow field.
- ii. Calculate the drag coefficient, lift coefficient, pressure coefficient, and skin friction factor.
- iii. Compare the results of the Spalart-Allmaras turbulence model with that of other well-known turbulence models.

The interest of the numerical simulation of this hydraulic issue is that the semi-circular cylinder is rotated by an angle from  $0^\circ$  to  $360^\circ$  in the water flow domain. Therefore, the impact of the rotation angle is considered for both points 1 and 2. Furthermore, this simulation deals with four different turbulent models in order to give perspective to the interaction between water flow and the semi-circular cylinder. The paper consists of four parts, these parts are methodology, results and discussion, comparative study and conclusions.

## 2. Methodology

In this section, we summarize in brief the geometric set up, boundary conditions, numerical method of turbulent model including governing equations of the solution, and mesh independency.

### 2.1 Geometric Set-up

Figure 1 gives complete details of the hydraulic problem geometric setup, including dimensions of the hydraulic domain and semi-circular cylinder dimensions, as well as the water flow direction. The geometric setup is done in a two-dimensional flow field using ANSYS Fluent software. Figure 1 involves the rotational angle of the semi-circular cylinder in the flow domain. In all cases, the flow is normal to the semi-circular cylinder regardless of the angle value. In other words, the flow is parallel to the longitudinal sides of the hydraulic domain. The water flow is an incompressible material with density and viscosity. Here, the distance which has been used between the upstream of hydraulic regime and rear face of semicircular cylinder equal to  $10D$ . This distance was used in many previous published works like Alonzo-García *et al.*, [15], Singha and Sinhamahapatra [16], Qasim and Jabbar [17], Qasim *et al.*, [18-20], and Jabbar *et al.*, [21,22]. In the present work, the distance between the upstream and the center of the cylinder is taken also as  $10D$ . Moreover, the turbulence in fluid flow results from the interaction between the walls and the layers of the flowing fluid. Therefore, the

amount of disturbance occurring does not depend on time, but rather depends primarily on the speed of flow (Reynolds number). Although turbulence means a change in flow properties such as speed, pressure, etc. over time, in models describing the turbulence occurring in these matters is done on the basis of their average value, plus the amount of oscillation occurring in them. In such cases, when one wants to describe any of the flow properties, the average value is taken for a specific period of time. From the above, it can be said that averaging a particular state for a specific period of time is equivalent to solving that problem as a steady state. Therefore, in this research, the problem is solved as a steady state. The boundary layer around the surface of cylinder remains laminar and the wake is completely turbulent for  $Re > 300$  [23]. Based on this information, we adopt steady state analysis.

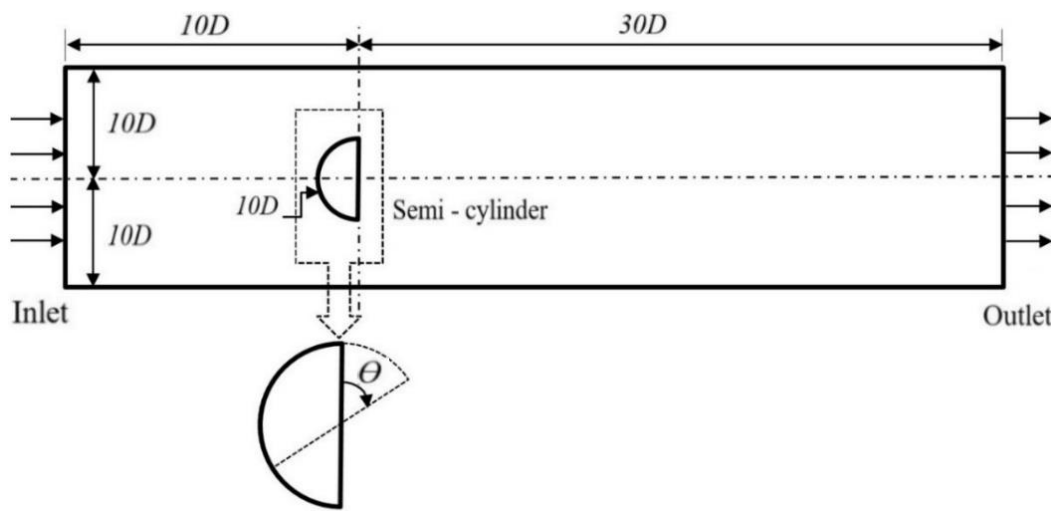


Fig. 1. The geometric set up of the hydraulic problem

## 2.2 The Boundary Conditions

Upstream flow velocity is adopted at the inlet, while at the outlet the pressure is set to zero gauge pressure. The no slip condition is applied between flow and the semi-circular cylinder as well no slip condition is applied between flow and the side walls.

## 2.3 The Governing Equations

The Reynolds-Averaged Navier-Stokes (RANS) set of equations for steady, incompressible flow of a fluid are given as:

$$\frac{\partial u_i}{\partial x_i} = 0 \tag{1}$$

$$\frac{\partial}{\partial x_i} (u_i u_j) = -\frac{\partial p}{\partial x_i} + \frac{\partial}{\partial x_i} \left[ \mu \left( \frac{\partial u_i}{\partial x_j} + \frac{\partial u_j}{\partial x_i} - \frac{2}{3} \delta_{ij} \frac{\partial u_l}{\partial x_l} \right) \right] + \frac{\partial}{\partial x_i} (-\rho \overline{u'_i u'_j}) \tag{2}$$

## 2.4 Numerical Method of Turbulent Models

The current simulations were achieved by adopting ANSYS software, four different turbulent models are used to perform the required solution of the hydraulic problem, and these turbulent models are:

### 2.4.1 Spalart-Allmaras model

This model is a relatively easy one-equation model [24]. The transported variable in this model,  $\tilde{\nu}$ , is identical to the turbulent kinematic viscosity except in the near-wall region. The value of  $\tilde{\nu}$  is:

$$\frac{\partial}{\partial X_i}(\rho \tilde{\nu} u_i) = G_\nu + \frac{1}{\sigma_{\tilde{\nu}}} \left[ \frac{\partial}{\partial X_i} \left\{ (\mu + \rho \tilde{\nu}) \frac{\partial \tilde{\nu}}{\partial X_i} \right\} + C_{b2} \rho \left( \frac{\partial \tilde{\nu}}{\partial X_i} \right)^2 \right] - Y_\nu + S_{\tilde{\nu}} \quad (3)$$

where  $G_\nu$  is the production of turbulent viscosity, and  $Y_\nu$  is the destruction of turbulent viscosity.  $\sigma_{\tilde{\nu}}$  and  $C_{b2}$  are the constants and  $\nu$  is the molecular kinematic viscosity.  $S_{\tilde{\nu}}$  is a user-defined source term. The turbulent viscosity,  $\mu_t$ , is computed from:

$$\mu_t = \rho \tilde{\nu} f_{\nu 1} \quad (4)$$

where  $f_{\nu 1} = \frac{\chi^3}{\chi^3 + C_{\nu 1}^3}$ ,  $\chi \equiv \frac{\tilde{\nu}}{\nu}$ . The production term,  $G_\nu$ , is modelled as:

$$G_\nu = C_{b1} \rho \tilde{S} \tilde{\nu} \quad (5)$$

where  $\tilde{S} = S + \frac{\tilde{\nu}}{\kappa^2 d^2} f_{\nu 1}$  and  $f_{\nu 2} = 1 - \frac{\chi}{1 + \chi f_{\nu 1}}$ . The terms  $\kappa$  and  $C_{b1}$  are constants,  $d$  is the distance from the wall, and  $S$  is a scalar measure of the deformation tensor. The destruction term  $Y_\nu$  is given by:

$$Y_\nu = C_{w1} \rho f_w \left( \frac{\tilde{\nu}}{d} \right)^2 \quad (6)$$

where  $f_w = g \left[ \frac{1 + C_{w3}^6}{g^6 + C_{w3}^6} \right]^{1/6}$ ,  $g = r + C_{w2}(r^6 - r)$ , and  $r \equiv \frac{\tilde{\nu}}{\tilde{S} \kappa^2 d^2}$ .

The model constants  $C_{b1}$ ,  $C_{b2}$ ,  $\sigma_{\tilde{\nu}}$ ,  $C_{\nu 1}$ ,  $C_{w1}$ ,  $C_{w2}$ ,  $C_{w3}$ , and  $\kappa$  have the following values  $C_{b1} = 0.1355$ ;  $C_{b2} = 0.622$ ;  $\sigma_{\tilde{\nu}} = \frac{2}{3}$ ,  $C_{\nu 1} = 7.1$ ;  $C_{w1} = \frac{C_{b1}}{\kappa^2} + \frac{(1 + C_{b2})}{\sigma_{\tilde{\nu}}}$ ;  $C_{w2} = 0.3$ ;  $C_{w3} = 2$ ,  $\kappa = 0.4187$ .

### 2.4.2 $k - \epsilon$ standard model

The standard  $k - \epsilon$  model is the simplest two-equation complete turbulence [25]. In this mode, the turbulence kinetic energy,  $k$ , and its rate of dissipation,  $\epsilon$ , are obtained from:

$$\frac{\partial}{\partial X_i}(\rho k u_i) = \frac{\partial}{\partial X_i} \left[ \left( \mu + \frac{\mu_t}{\sigma_k} \right) \frac{\partial k}{\partial X_i} \right] + G_k + G_b - \rho \epsilon - Y_M + S_k \quad (7)$$

$$\frac{\partial}{\partial X_i}(\rho \epsilon u_i) = \frac{\partial}{\partial X_i} \left[ \left( \mu + \frac{\mu_t}{\sigma_\epsilon} \right) \frac{\partial \epsilon}{\partial X_i} \right] + C_{1\epsilon} \frac{\epsilon}{k} (G_k + C_{3\epsilon} G_b) - C_{2\epsilon} \rho \frac{\epsilon^2}{k} + S_\epsilon \quad (8)$$

where  $G_k$  is the generation of the turbulence kinetic energy,  $G_b$  is the generation of the turbulence kinetic energy due to buoyancy,  $Y_M$  denotes the influence of the fluctuating dilatation in compressible turbulence to the total dissipation rate,  $\sigma_k$  and  $\sigma_\epsilon$  are the turbulent Prandtl numbers,  $S_k$  and  $S_\epsilon$  are source terms defined by the user. The terms  $C_{1\epsilon}$ ,  $C_{2\epsilon}$  and  $C_{3\epsilon}$  are constants.

The turbulent viscosity  $\mu_t$  is calculated by combining  $k$  and  $\epsilon$  as follows:

$$\mu_t = \rho C_\mu \frac{k^2}{\varepsilon} \quad (9)$$

The model constants  $C_{1\varepsilon}$ ,  $C_{2\varepsilon}$ ,  $C_\mu$ ,  $\sigma_k$  and  $\sigma_\varepsilon$  are equal respectively to 1.44, 1.92, 0.09, 1, and 1.3.

#### 2.4.3 $k - \varepsilon$ (RNG) model

The RNG  $k - \varepsilon$  turbulence model is created from the instantaneous Navier-Stokes equations by means of a mathematical technique called renormalization group RNG methods [26]. The RNG  $k - \varepsilon$  model has an identical formula to the standard model:

$$\frac{\partial}{\partial X_i} (\rho k u_i) = \frac{\partial}{\partial X_i} \left[ \alpha_k \mu_{eff} \frac{\partial k}{\partial X_i} \right] + G_k + G_b - \rho \varepsilon - Y_M + S_k \quad (10)$$

$$\frac{\partial}{\partial X_i} (\rho \varepsilon u_i) = \frac{\partial}{\partial X_i} \left[ \alpha_\varepsilon \mu_{eff} \frac{\partial \varepsilon}{\partial X_i} \right] + C_{1\varepsilon} \frac{\varepsilon}{k} (G_k + C_{3\varepsilon} G_b) - C_{2\varepsilon} \rho \frac{\varepsilon^2}{k} - R_\varepsilon + S_\varepsilon \quad (11)$$

The scale elimination procedure results in a differential equation for turbulent viscosity:

$$d \left( \frac{\rho^2 k}{\sqrt{\varepsilon \mu}} \right) = 1.72 \frac{\hat{\nu}}{\sqrt{\hat{\nu}^3 - 1 + C_\nu}} d\hat{\nu} \quad (12)$$

where:  $\hat{\nu} = \frac{\mu_{eff}}{\mu}$  and  $C_\nu \approx 100$ . The model constants are  $C_{1\varepsilon} = 1.42$  and  $C_{2\varepsilon} = 1.68$ .

#### 2.4.4 $k - \varepsilon$ realizable model

The modelled transport equations for  $k$  and  $\varepsilon$  in the realizable model are [27]:

$$\frac{\partial}{\partial X_j} (\rho k u_j) = \frac{\partial}{\partial X_j} \left[ \left( \mu + \frac{\mu_t}{\sigma_k} \right) \frac{\partial k}{\partial X_j} \right] + G_k + G_b - \rho \varepsilon - Y_M + S_k \quad (13)$$

$$\frac{\partial}{\partial X_j} (\rho \varepsilon u_j) = \frac{\partial}{\partial X_j} \left[ \left( \mu + \frac{\mu_t}{\sigma_\varepsilon} \right) \frac{\partial \varepsilon}{\partial X_j} \right] + \rho C_1 S_\varepsilon - \rho C_2 \frac{\varepsilon^2}{k + \sqrt{\nu \varepsilon}} + C_{1\varepsilon} \frac{\varepsilon}{k} C_{3\varepsilon} \varepsilon G_b + S_\varepsilon \quad (14)$$

The modeling of the turbulent viscosity is done as in other  $k - \varepsilon$  models, where the eddy viscosity  $\mu_t$  is calculated from:

$$\mu_t = \rho C_\mu \frac{k^2}{\varepsilon} \quad (15)$$

where  $C_1 = \max \left[ 0.43, \frac{\eta}{\eta + 5} \right]$ ,  $\eta = S \frac{k}{\varepsilon}$ ,  $S = \sqrt{2 S_{ij} S_{ij}}$ , and  $S_{ij} = \frac{1}{2} \left( \frac{\partial u_i}{\partial X_j} - \frac{\partial u_j}{\partial X_i} \right)$ .

The model constants  $C_{1\varepsilon}$ ,  $C_2$ ,  $\sigma_k$  and  $\sigma_\varepsilon$  are equal to 1.44, 1.9, 1, and 1.2 respectively [27].

#### 2.5 Drag Coefficient, lift Coefficient, and pressure coefficient

The drag coefficient,  $CD$ , is defined as:

$$CD = \frac{F_D}{\frac{1}{2} \rho U_\infty^2 A_{ref}} \quad (16)$$

where,  $F_D$  is the drag force,  $U_\infty$  is the free-stream velocity,  $A_{ref}$  is the reference area measured in square meters.

Now, we deal with the calculation of the semi-circular cylinder projection area (reference area), which is adopted in the current study. For unit depth, the reference area (see Table 1):

$$A_{ref} = Y1 + Y2 \tag{17}$$

For the range  $0^\circ \leq \theta \leq 180^\circ$ ,  $Y1$  is equal to the radius of the cylinder and  $Y2$  is given by:

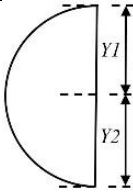
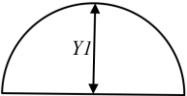
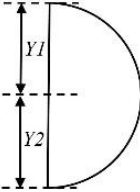
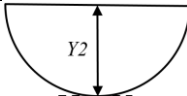
$$Y2 = R |\cos(\theta)| \tag{18}$$

While for the range  $180^\circ \leq \theta \leq 360^\circ$ ,  $Y2$  is equal to the radius of the cylinder and  $Y1$  is given by:

$$Y1 = R |\cos(\theta)| \tag{19}$$

We summarize the details of  $Y1$ ,  $Y2$  and  $A_{ref}$  for four selected angles in Table 1.

**Table 1**  
 The reference area for drag coefficient

$\theta = 0^\circ$	$\theta = 90^\circ$	$\theta = 180^\circ$	$\theta = 270^\circ$
			
$Y1 = R$ $Y2 = R$ $A_{ref} = 2R$	$Y1 = R$ $Y2 = 0$ $A_{ref} = R$	$Y1 = R$ $Y2 = R$ $A_{ref} = 2R$	$Y1 = 0$ $Y2 = R$ $A_{ref} = R$

Concerning lift coefficient,  $CL$ , it is defined by:

$$CL = \frac{F_L}{\frac{1}{2}\rho U_\infty^2 A_{ref}} \tag{20}$$

where  $F_L$  is the lift force.

The reference area (wing area) in this case is related to  $x1$  and  $x2$  as shown in Table 2:

$$A_{ref} = x1 + x2 \tag{21}$$


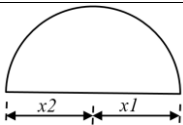

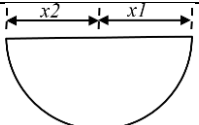
For the range  $0^\circ \leq \theta \leq 180^\circ$ , then  $x2$  is equal to the radius of the cylinder  $R$  and  $x1$  is given by:

$$x1 = R |\sin(\theta)| \tag{22}$$

While for the range  $180^\circ \leq \theta \leq 360^\circ$ , then  $x1$  is equal to the radius of the cylinder and  $x2$  is given by:

$$x2 = R |\sin(\theta)| \tag{23}$$

**Table 2**  
 The reference area for lift coefficient

$\theta = 0^\circ$	$\theta = 90^\circ$	$\theta = 180^\circ$	$\theta = 270^\circ$
			
$x1 = 0$ $x2 = R$ $A_{ref} = R$	$x1 = R$ $x2 = R$ $A_{ref} = 2R$	$x1 = R$ $x2 = 0$ $A_{ref} = R$	$x1 = R$ $x2 = R$ $A_{ref} = 2R$

The pressure distribution is well described and understood by using the pressure coefficient,  $CP$ , which is defined by:

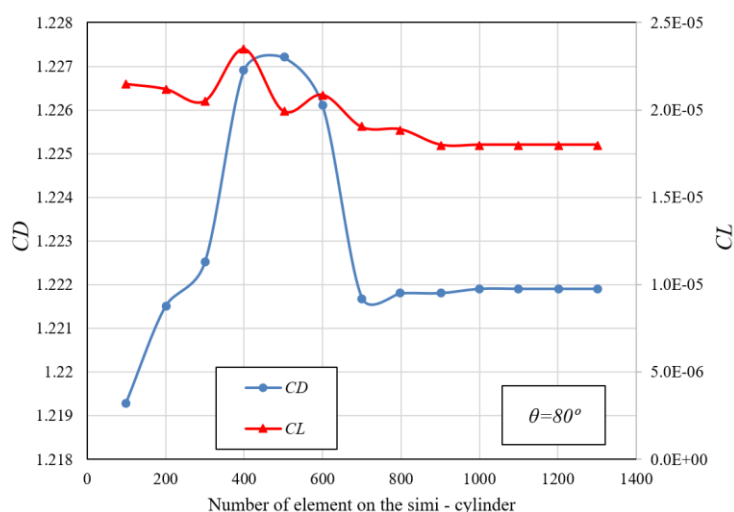
$$CP = \frac{P - P_{atm}}{\frac{1}{2} \rho U_\infty^2} \quad (24)$$

where  $P$  is the pressure at any point on the body is surface and  $P_{atm}$  is the atmospheric pressure.

### 2.6 Mesh Independence

Before explaining the mesh independence test, we must mention here that the structure mesh tool is used for highly accurate meshing. Inflation and edge size were adopted on the edge and near of the cylinder to dense mesh structures. After the mesh was generated, the setup fluent ANSYS 2020 ran at steady state. Pressure base was used for incompressible fluid. The second-order upwind scheme is applied to discretize the momentum equations for a more accurate solution.

Figure 2 shows the relation between the number of elements around the semi-circular cylinder circumference and both drag coefficient and lift coefficient. It is seen from the figure that after 1000 elements, then both of the coefficients remain constant without any variation regardless of the increase in the of elements. Therefore, the number of elements equal to 1000 is adopted in the current study. Figure 3 shows the elements distribution in the hydraulic domain and where the dense elements became concentrated.



**Fig. 2.** The variation of drag coefficient and lift coefficient with the number of elements



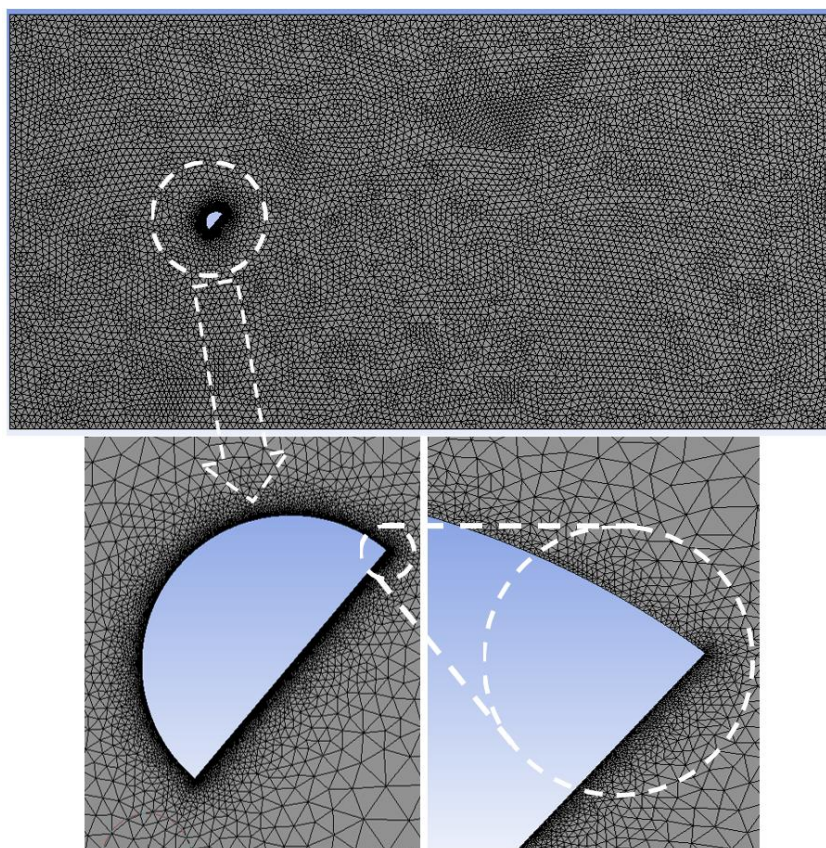


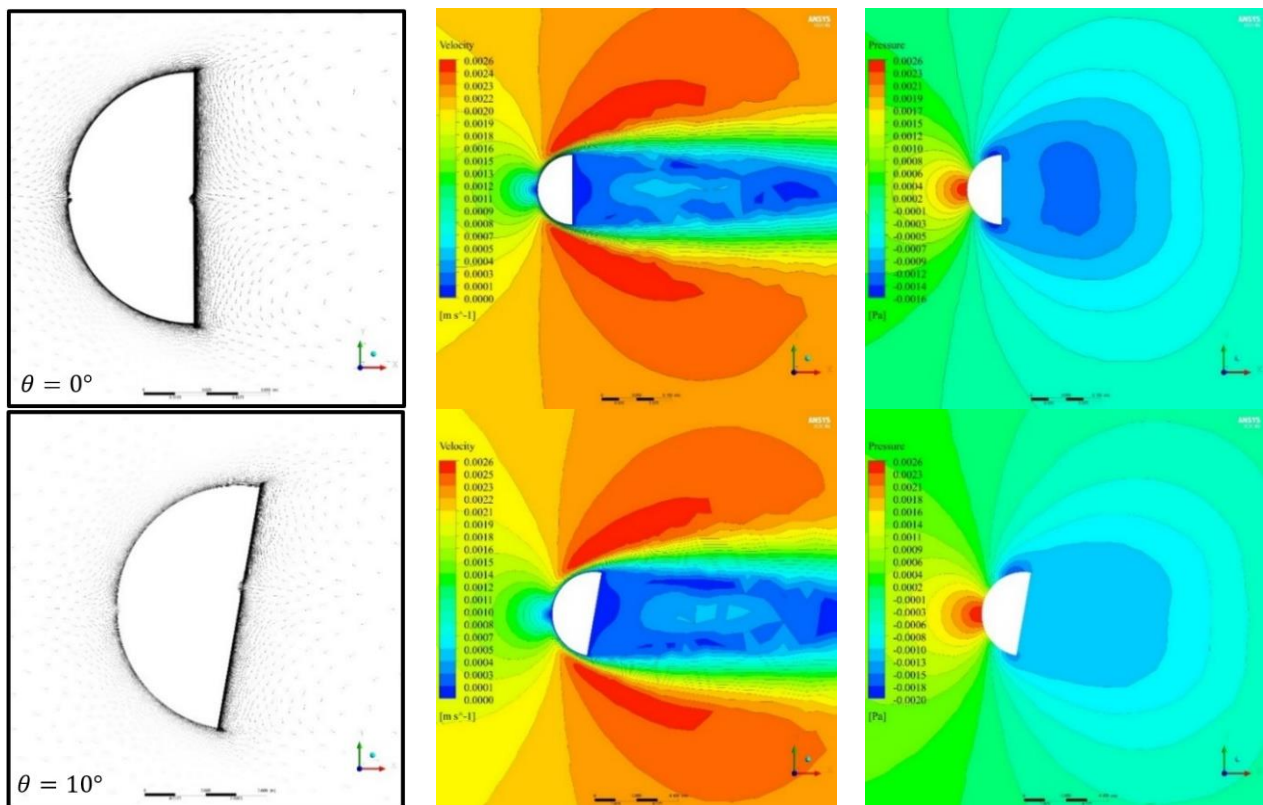
Fig. 3. The element mesh distribution in the hydraulic domain

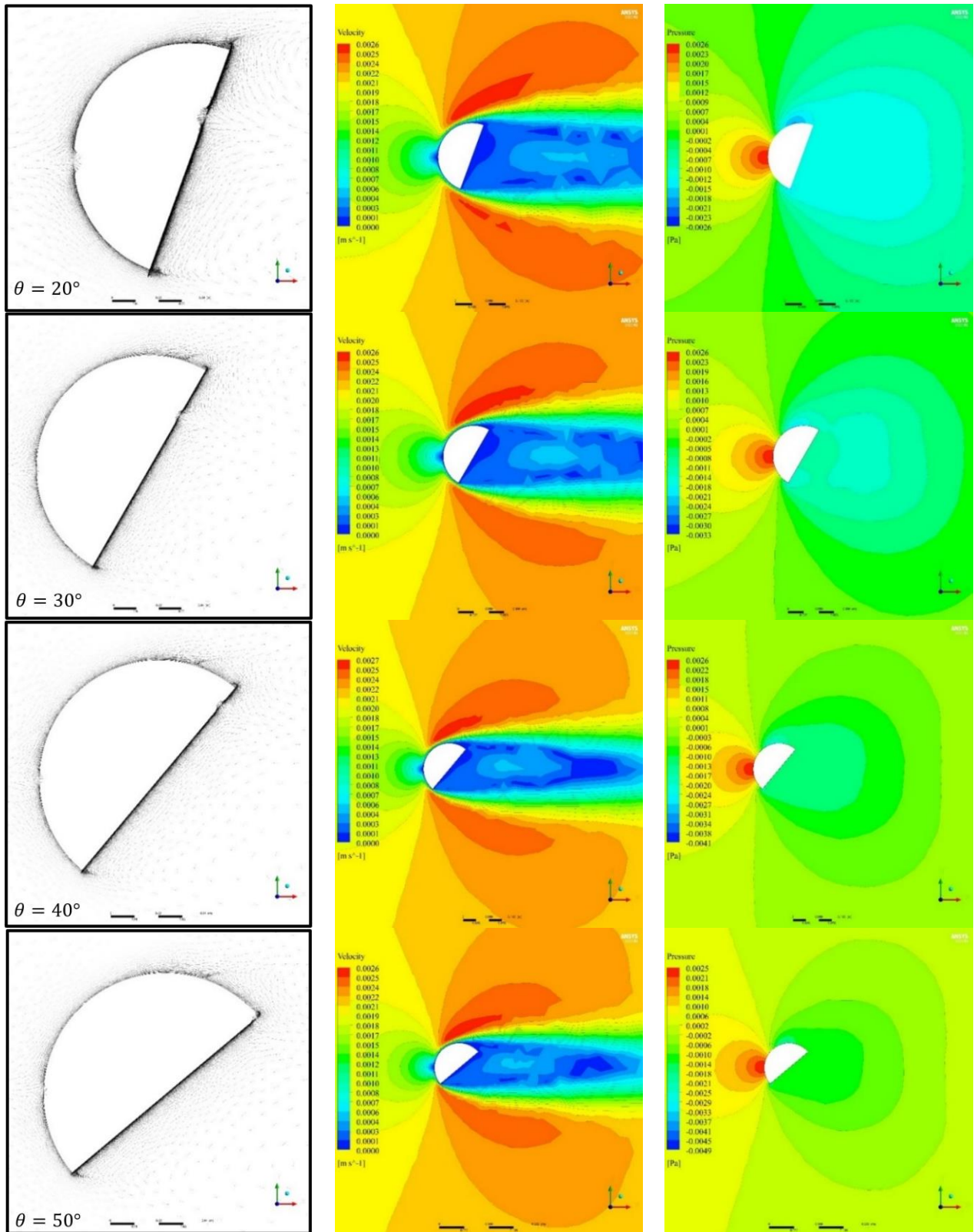
### 3. Results and Discussion

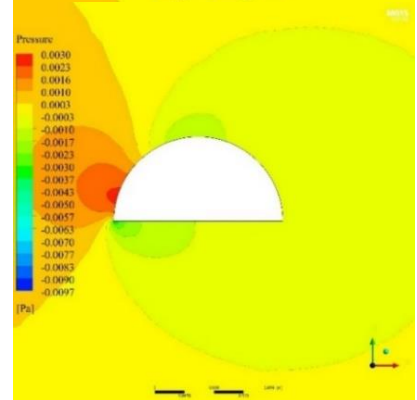
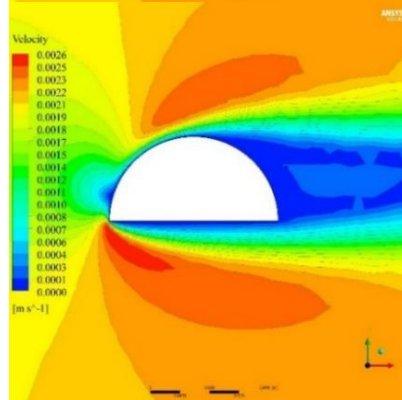
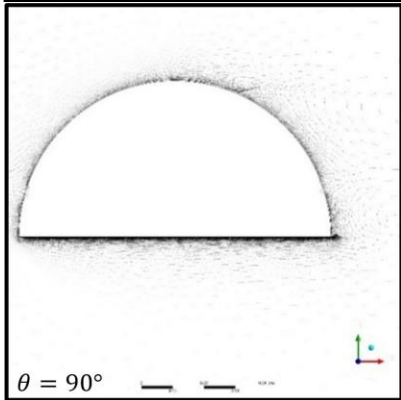
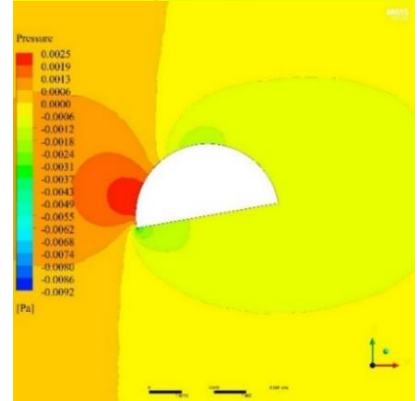
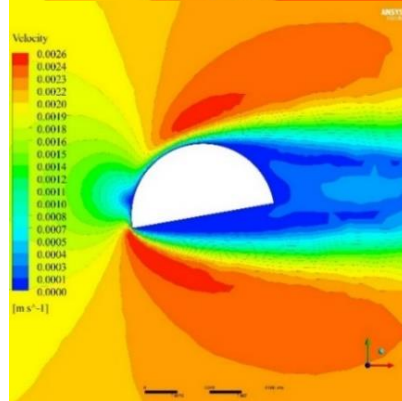
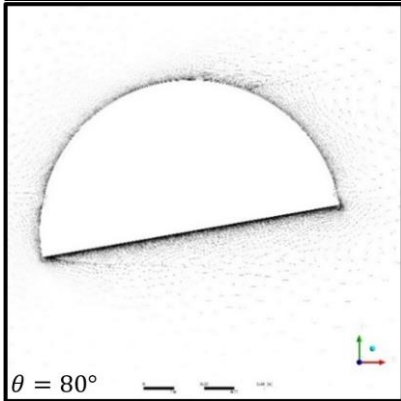
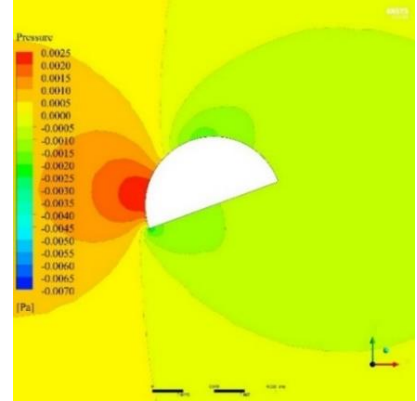
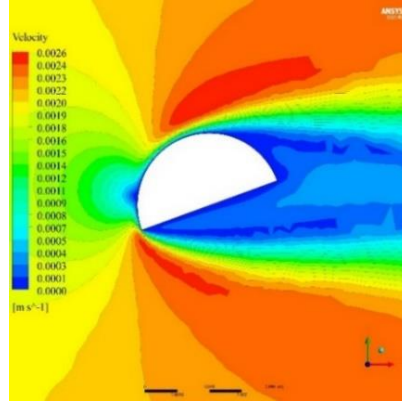
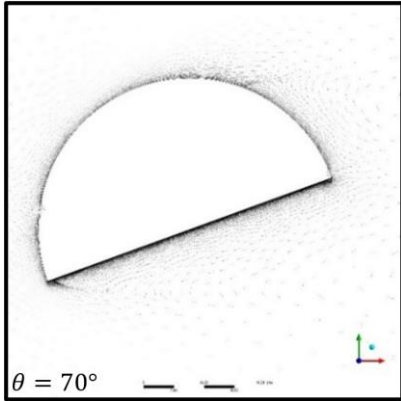
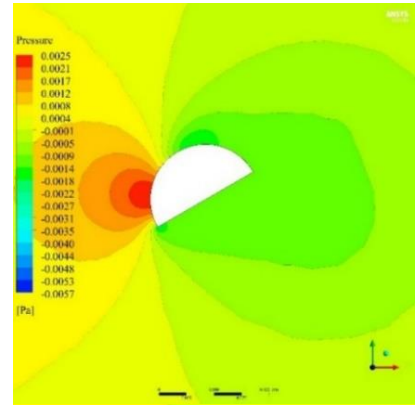
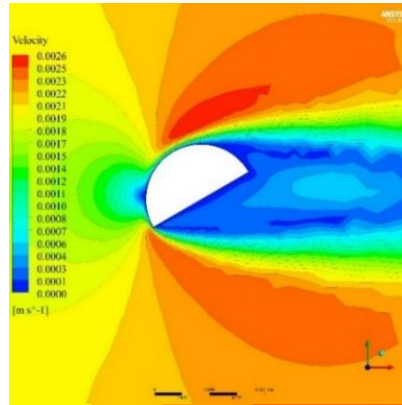
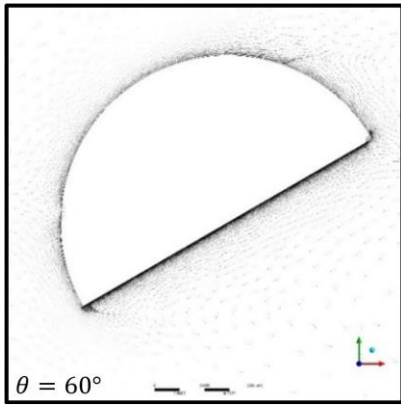
This study deals with investigating the flow around a semi-circular cylinder in two dimensions. Here, the cylinder is considered stationary and placed in the domain with different orientations. Rotation angle are varied from  $0^\circ$  to  $360^\circ$  and two values of Re number are considered, 2653.9 and 26539. Figure 4 consists of three parts, velocity vector, velocity contour, and pressure contour. The distributions of all the previous hydraulic variables are plotted for different angles; these angles are referred as the rotational angle of a semi-circular cylinder in the water field. These angles range from zero to  $180^\circ$  to introduce a good reasonable and feasible description of the water field, which is surrounding a semi-circular cylinder. The velocity patterns and pressure patterns are calculated by the Spalart-Allmaras model.

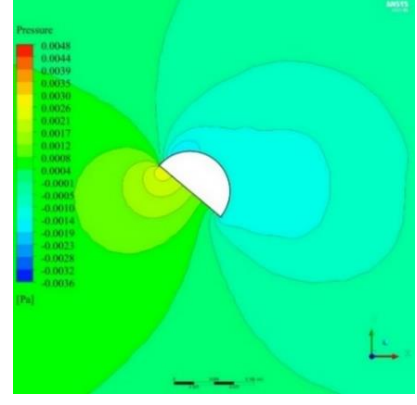
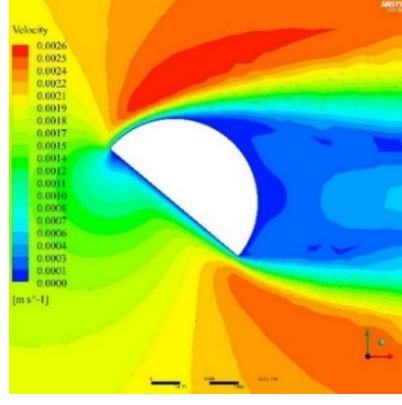
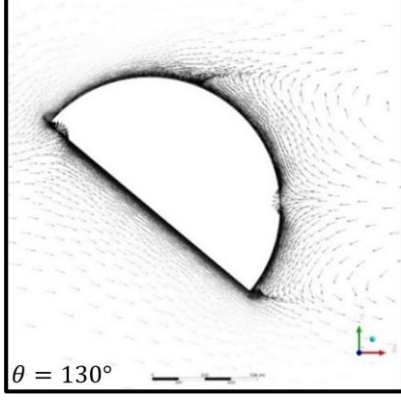
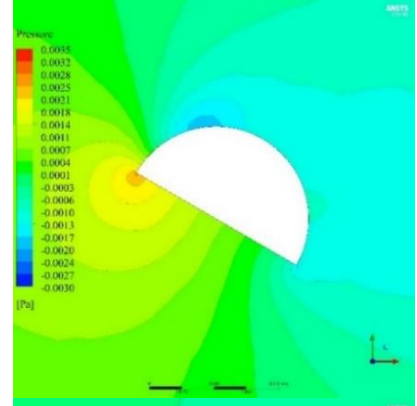
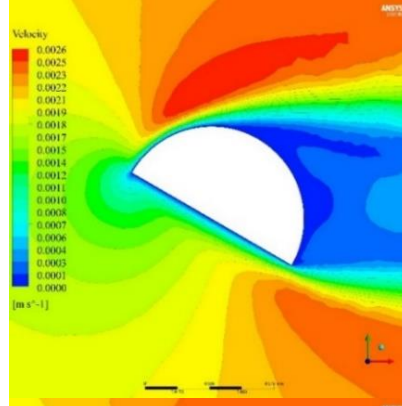
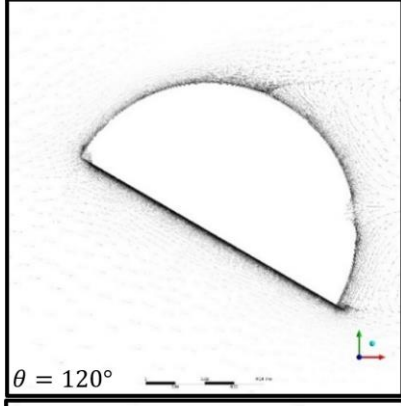
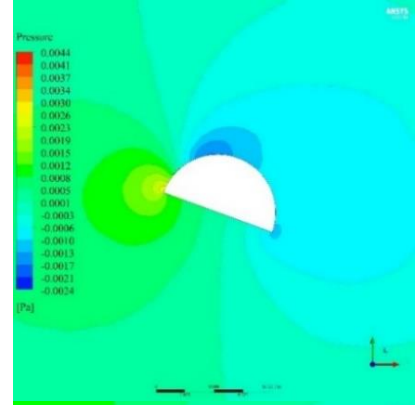
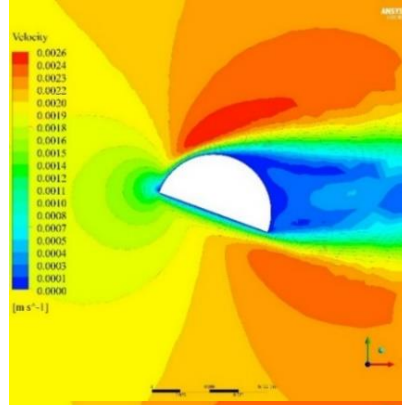
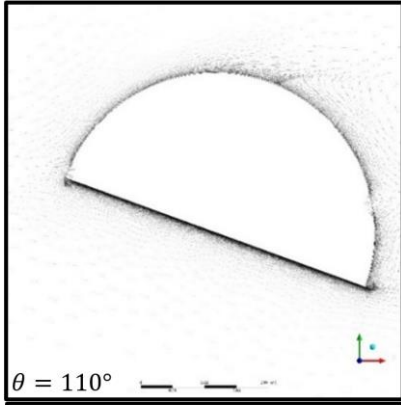
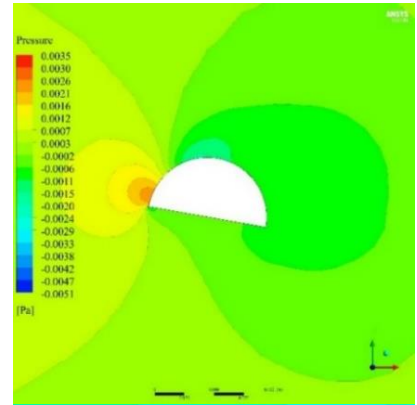
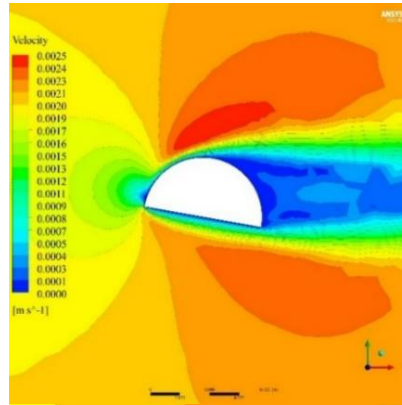
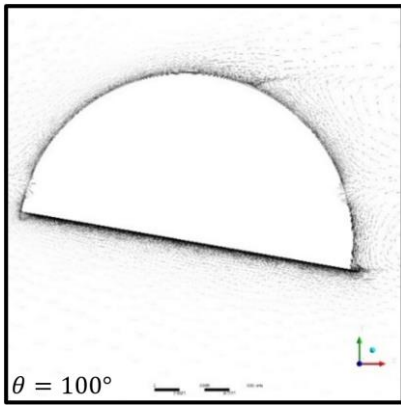
The discussion relies on two major items; flow direction relative to the cylinder and the position of the stagnation points. Here, two stagnation points must be recognized, the first at the head portion of the cylinder and called the forward stagnation point, while the second called the base point. Due to the variation in the values of the angle, both points will move depending on angle value relative to the water flow. Regarding the velocity vector, for cases when the rotation angles ranges from zero to  $90^\circ$ , for an angle equal to zero, when the flow strikes the cylinder leading part. Here, the flow will divide into two parts: one part goes to the right side of the cylinder, while the other goes to the left side. At the cylinder's rear part, the flow recirculated at downstream of the cylinder. The interesting point will relate to the position of the stagnation points. Both stagnation points approximately lay at the same line. When the angle is equal to  $10^\circ$ ,  $20^\circ$ , and  $30^\circ$  the flow behavior is similar to the flow behavior when the angle is equal to zero. For angles above  $30^\circ$  (from  $40^\circ$  to  $80^\circ$ ), the recirculation of the flow moves toward the curve portion of the cylinder and this appears clearly, at angle  $90^\circ$  the

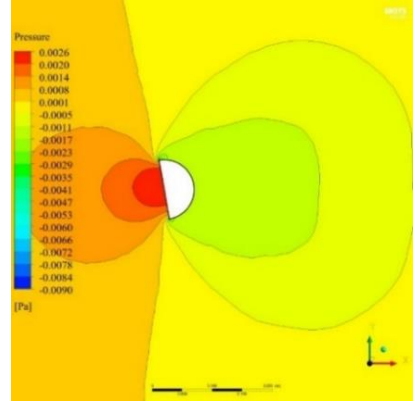
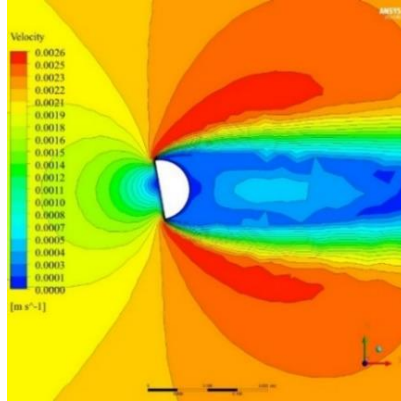
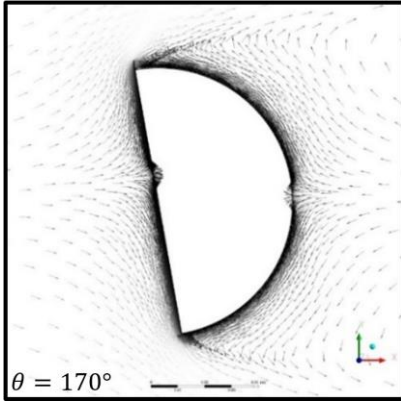
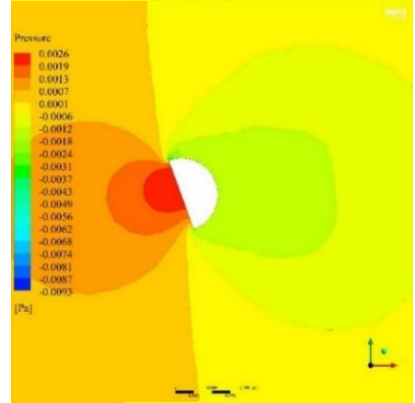
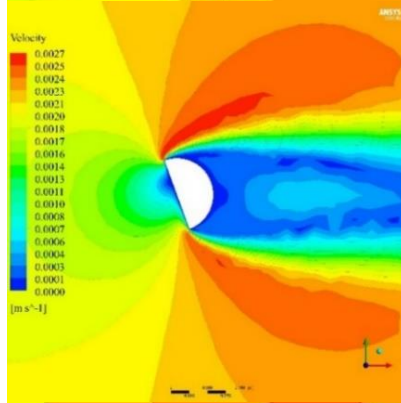
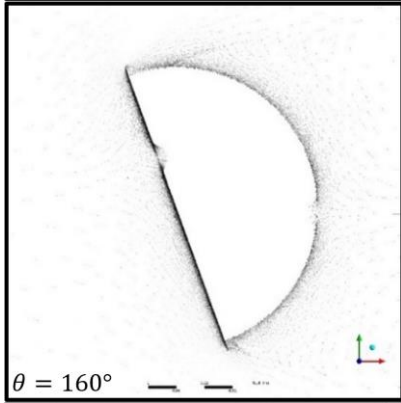
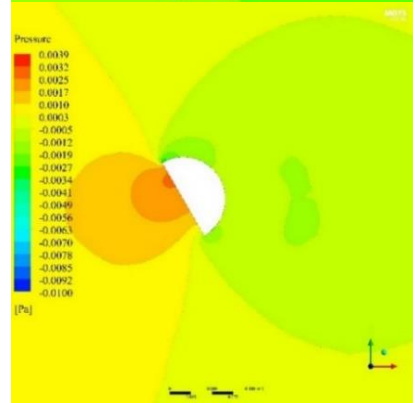
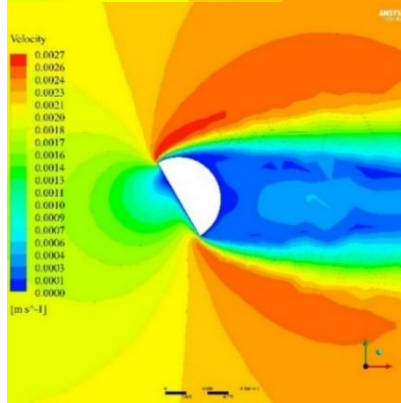
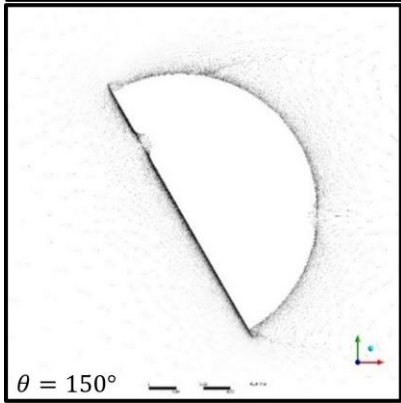
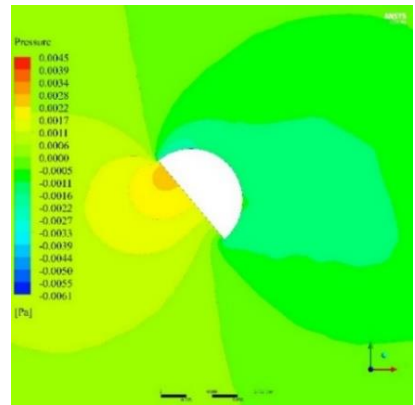
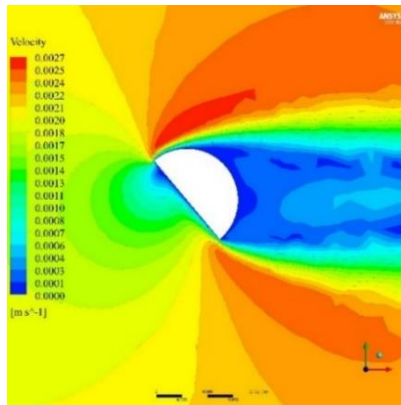
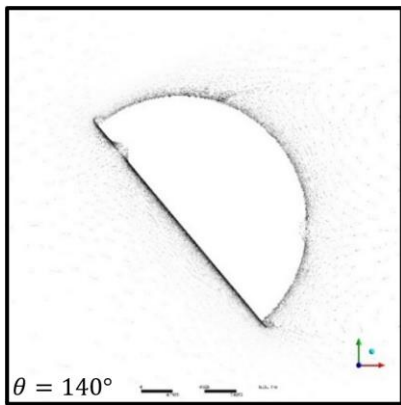
flow behavior is similar to the flow around the cylinder when the angle is equal to zero. As the angle increases, both stagnation points will move and the difference in the location of the two points appears clearly. When the angle values from  $100^\circ$  to  $170^\circ$ , the flow behavior is similar to the flow behavior when the angle values from  $40^\circ$  to  $80^\circ$ . The remarkable point of the problem appears clearly at angle  $180^\circ$ , when the flow behavior is similar to the flow behavior when the angle is equal to zero and  $90^\circ$ . Also, at angle  $180^\circ$  both stagnation points lay at the same line. When the angle equals to  $190^\circ$ , the flow behavior is similar to the flow behavior when angle values from  $40^\circ$  to  $80^\circ$ . The congruence in the flow velocity vector relies mainly on the angle values; also, these values have a direct impact on the location of the stagnation points. The velocity vector alteration depends on the separation points. Here, it is important to recognize two different types of separation points, mobile separation points and fixed separation points. For the curve portion of the semi-circular cylinder, the separation points are considered mobile points, regardless of the values of the angle. As the semi-circular cylinder rotates by an angle, the straight line of the cylinder becomes inclined. Consequently, the separation points on the inclined line are considered mobile points. The angle of rotation has a direct effect on the boundary layer detachment, therefore as detachment increases, the flow separation will increase too. For the velocity contour, a positive flow field surrounds the semi-circular cylinder in all directions, the location of the flow separation appears clearly in Figure 4, and this zone is around the solid boundary along the cylinder perimeter. For the pressure field, which surrounds the semi-circular cylinder changes from positive to negative depending on the values of the angle. When the angle is equal to zero, the positive pressure is surrounded along the portion of the cylinder perimeter as compared with negative pressure, when the angle ranges from  $10^\circ$  to  $190^\circ$  the negative pressure surrounded along portion of the cylinder as compared with positive pressure. The variation in both velocity and pressure field appears clearly due to the inversely proportional relationship between them. Here, we must mention that as the cylinder rotation angle increases, the angle of attack between flow and cylinder will change.











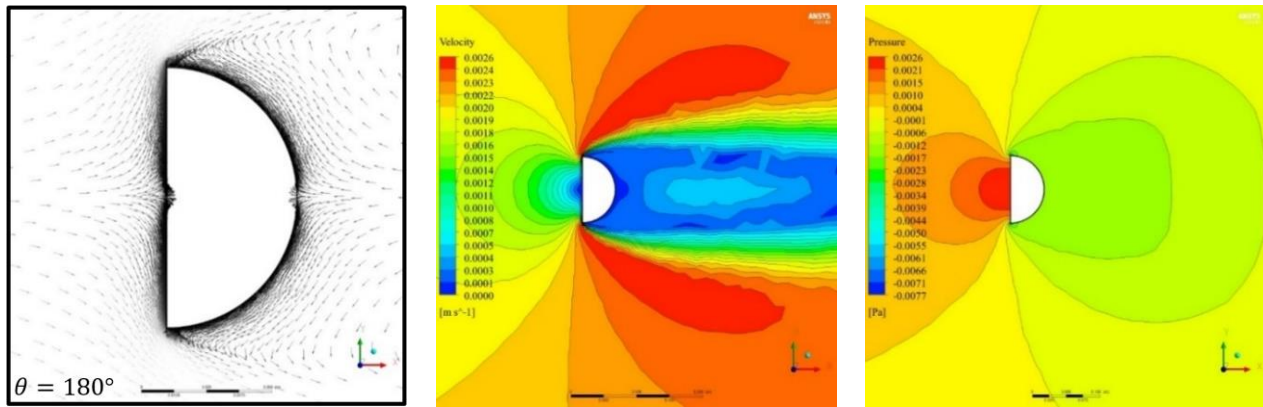
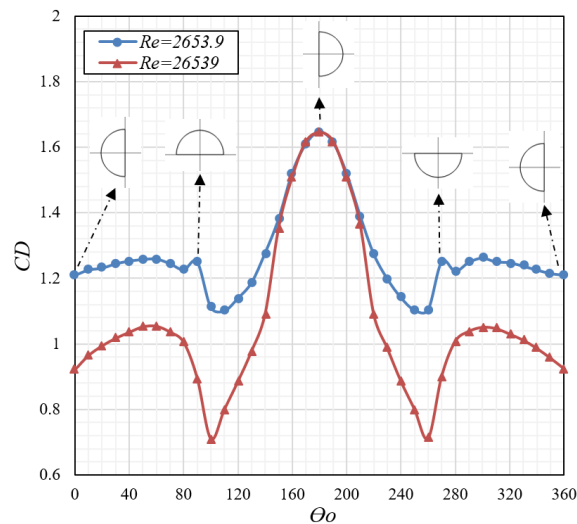


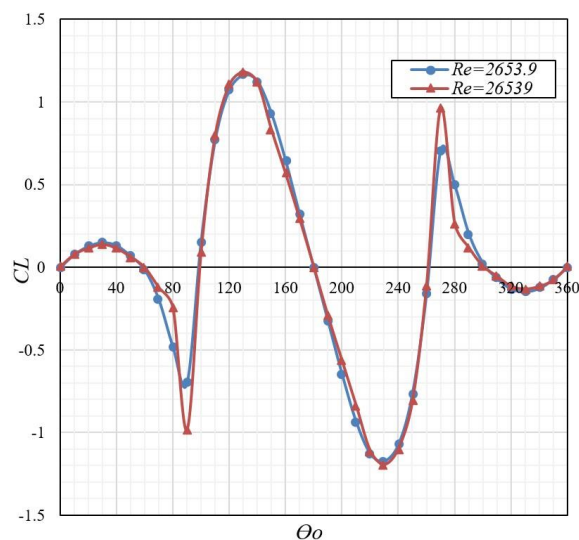
Fig. 4. Velocity vector, velocity contour, and pressure contour for different angles of rotation

Figure 5 shows the relation between drag coefficient and angle of rotation. This relation is built by the Spalart-Allmaras turbulent model. The numerical computation for the trend in the relationship between the two dimensionless parameters is based on two different Reynolds numbers. The first  $Re=2653.9$  and the second  $Re=26539$ . Here, the second Reynolds number is greater than the first by tenfold. Also, Figure 5 shows a nonlinear and harmonic relationship between the two investigated parameters. The two curves are symmetrical about the angle  $180^\circ$ , have the same behavior, and have the same shape regardless of the angle values. The two curves depend on the values of the Reynolds number. When the Reynolds number increases, then the drag coefficient will decrease, because of flow separation. This is applicable to the second curve, where the Reynolds number is greater than the first curve by tenfold and this leads to reduction in the values of the drag coefficient of the second curve. This clarification is allowable when the range of angle from zero to  $150^\circ$  and from  $210^\circ$  to  $360^\circ$ . When the angle range between  $160^\circ$  and  $220^\circ$  then both curves are congruent or identical regardless the difference in Reynolds number values. This happens because the separation of flow occurs at the sharp corner (point of meeting between line and curve) and the separations point are considered fixed and considered independent of Reynolds number values, therefore, both curves are similar. For both curves, the variation in drag coefficient depends on the viscous effect. Generally, the drag coefficient relies on the flow velocity and frontal area of the body (projection area), so for any curves (curve 1 or curve 2) the flow velocity is considered constant, therefore the frontal area has a major influence on the values of the drag coefficient owing to inverse proportion between drag coefficient and frontal area of the body. Furthermore, the drag coefficient is influenced by the angle of cylinder rotation because of this angle is used to calculate the frontal area. In addition, the figure gives the values of peak, maximum, and minimum with the variation of the angle values.



**Fig. 5.** Relationship between drag coefficient and rotation angle

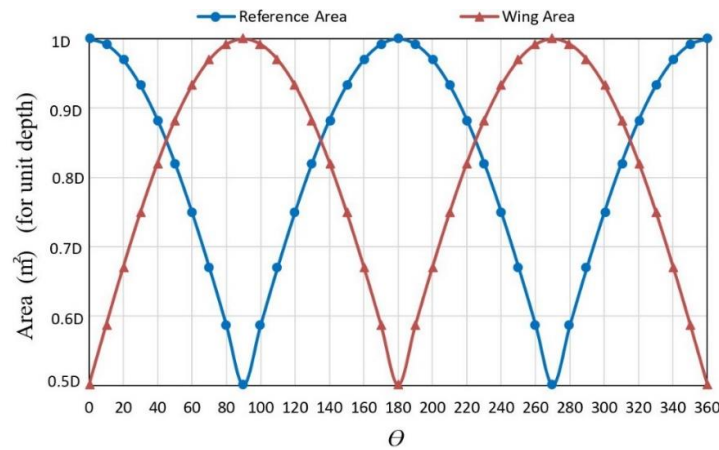
Figure 6 shows the relation between lift coefficient and angle of rotation. This relation is built by the Spalart-Allmaras turbulent model. The numerical computation for the trend in the relationship between the two dimensionless parameters is based on two different Reynolds numbers. The first  $Re=2653.9$  and the second  $Re=26539$ . Here the second Reynolds number is greater than the first by tenfold. Figure 6 produces nonlinear and harmonic relationship between the two investigated parameters. The two curves are symmetrical about the angle  $180^\circ$  and have the same behavior and shape regardless of the angle values. In addition, the two curves are identical. From the two curves, we infer that the lift coefficient is independent of Reynolds numbers values. From the figure, the lift coefficient has zero value when the angle is equal to zero and  $360^\circ$  because the flow is normal to the semi-circular cylinder. When the semi-circular cylinder makes an angle with flow direction, the lift coefficient values will fluctuate between positive and negative values respectively. In addition, the flow pattern around a semi-circular cylinder becomes non-symmetrical. Here, this angle leads to differences in pressure distribution on the upper part and lower part of a semi-circular cylinder, so this will reflect directly on the values of the lift coefficient.



**Fig. 6.** Relationship between lift coefficient and rotation angle



For more clarification, for angle values between zero and  $60^\circ$ , it is shown from Figure 7 that the projection area will decrease when the angle values from zero to  $60^\circ$ . As the projection area decreases, the drag coefficient will be increased due to the inverse proportion between drag coefficient and projection area according to Eq. (16). For angle values between  $60^\circ$  and  $90^\circ$ , Figure 7 shows that the projection area will decrease.

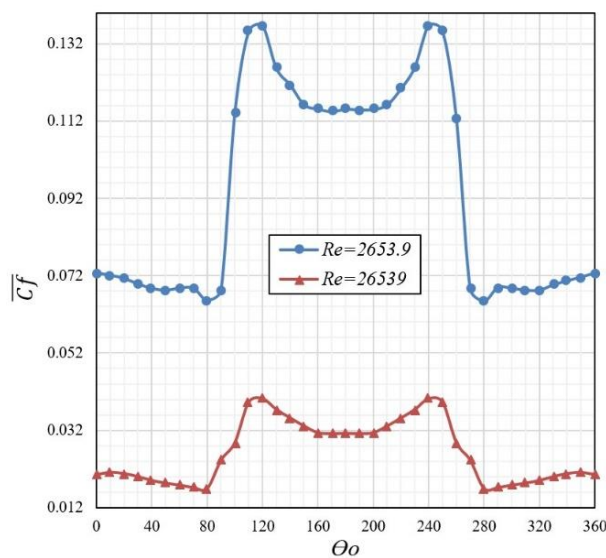


**Fig. 7.** Relationship between the reference area and rotation angle

In addition, the drag coefficient will be reduced too because of the drag force, which is exerted in the semi-circular cylinder and this will reflect directly on the values of the drag coefficient owing to the direct proportion between drag coefficient and drag force according to the Eq. (16). For angle values between  $90^\circ$  and  $100^\circ$  degree, the drag coefficient will decrease while for angle between  $100^\circ$  to  $130^\circ$  the drag coefficient will increase. Also, when angle values from  $90^\circ$  to  $100^\circ$  the projection area will decrease while, for angle value from  $100^\circ$  to  $130^\circ$  the projection area will increase, therefore, we infer that both the drag force and the projection area will dominate the values of the drag coefficient. For angle values between 130 and 180 degrees, the drag coefficient is increased suddenly. Also, from Figure 7, for angles values from  $130^\circ$  to  $180^\circ$ , the projection area will increase with the angle. Here, in this case, the drag force is considered great and dominates the values of the drag coefficient owing to the direct proportion between them based on Eq. (16) and the projection area has no direct effect. The same behavior is shown for the remaining portion of the curve shown in Figure 5 owing to the curve being symmetrical about the angle  $180^\circ$ . Also, from Figure 7, for angle values from zero to  $30^\circ$ , the lift coefficient and the wing area are increase gradually. Here, the lift coefficient is more affected by lift force owing to the direct proportion between them according to Eq. (20). In this situation, the lift force is high as compared with the wing area. For angle values from  $40^\circ$  to  $90^\circ$ , the lift coefficient decreases gradually, also for the same values of angle the wing area increases gradually. As the wing area decreases, the lift coefficient increases due to the inverse proportion between them according to the Eq. (20). For angle values from  $100^\circ$  to  $130^\circ$ , the lift coefficient increases with the angle values. Here, the wing area decreases with increasing the angle value, as the wing area decreases the lift coefficient increases owing to the inversely proportional between them. Also, for angle values from  $130^\circ$  to  $180^\circ$ , the lift coefficient decreases sharply with increasing in the angle values. Here, the wing area increases with increasing the angle value, as the wing area increases the lift coefficient decreases owing to the inversely proportional between them. The same behavior is shown for the remain portion of the curve shown in Figure 7. As well, Figure 7 shows an interesting relationship between the effective area of the semi-circular cylinder and various

values of the angle. Here, the effective area is pointed to the projection area of the semi-circular cylinder which shares in the calculation of the drag coefficient and this area has inverse proportion with drag coefficient. Therefore, any increase or decrease in this area will be reflected directly on the values of the drag coefficient without any contrast. While in the lift coefficient, the effective area is pointed to wing area and this is responsible for the control of the value of the lift coefficient. This area has inverse proportion with lift coefficient without any contrast. The projection area is considered normal to the flow direction while wing area is considered parallel to the flow direction. Here, because of the significant influence of the effective area, it is important to remark that the difference that occurs in both values of drag and lift coefficients is related to the rise in the values of drag and lift forces respectively.

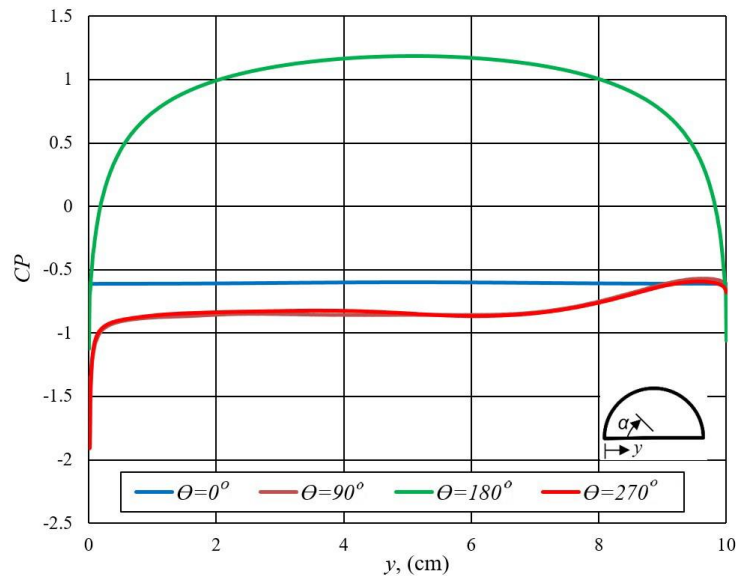
Figure 8 shows the relationship between the skin friction factor and the angle of rotation, which is built by Spalart-Allmaras turbulent model. The numerical computation for the trend relationship in the between the two dimensionless parameters is based on two different Reynolds numbers. The first is  $Re=2653.9$  and the second is  $Re=26539$ . Here the second Reynolds number is greater than the first by tenfold. Figure 8 produces nonlinear and harmonic relationships between the two investigated parameters. The two curves are symmetrical about the angle  $180^\circ$  and have the same behavior and shape regardless of the angle values. It is obvious from the Figure 8 that Reynolds number has a major impact on the determination the values of the skin friction factor. As Reynolds number increase, the skin friction factor decreases. The contrast in the values of the skin friction factors is based on the flow velocity and the area of the cylinder, which has direct contact with fluid, so these two variables will dominate the values of the skin friction factor. As well, the angle has an important effect in the determination of the skin friction factor because it shares in the determination of the cylinder area that has a direct contact with the fluid.



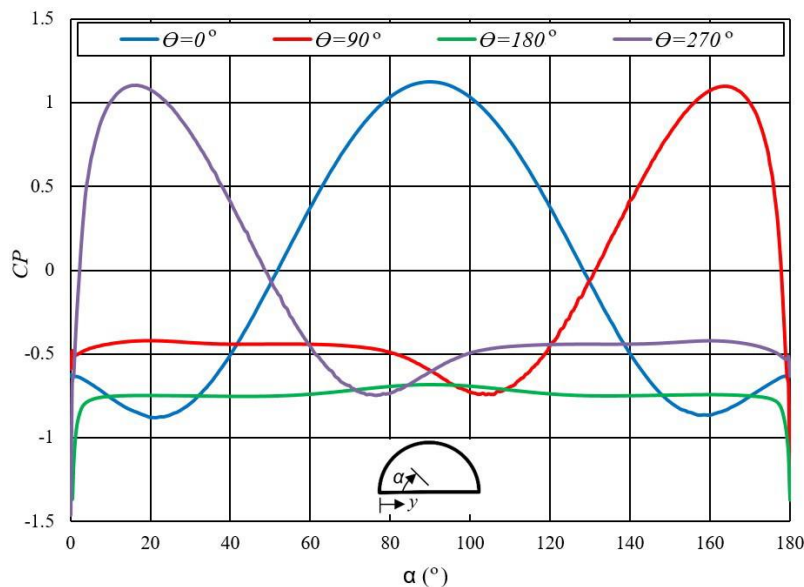
**Fig. 8.** The trend in the relationship between skin friction factor and rotation angle

Both Figure 9 and Figure 10 have been plotted for  $Re = 2653.9$ . For Figure 9, the pressure coefficient values change from positive to negative or adverse. When the angle is equal to 90 degree or 270 degree, both curves are identical, while for an angle equal to zero the curve is symmetrical around angle 90 degree and all the values of pressure coefficient are negatives for angle 180 degree. In general, this behavior is attributed to the change in flow separation along the curve of the semicircular cylinder which rely on the orientation angle of the semicircular cylinder. In other word,

the alteration in the flow angle attack has a direct impact on the pressure coefficient values. Figure 10, for all the selected angles the pressure coefficient values are negative except for angle 180 degree in which the pressure coefficient is changed from negative to positive or adverse and this occurs. Here, the values of the pressure coefficient rely on flow separation. For the flow beside the straight line, fixed separation point of flow occurs at the corner where the curve portion and straight line portion intersect.



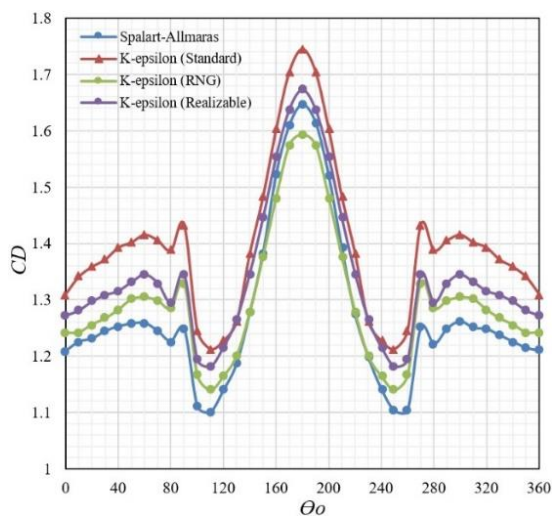
**Fig. 9.** Variation of pressure coefficient at the straight surface at  $Re = 2653.9$



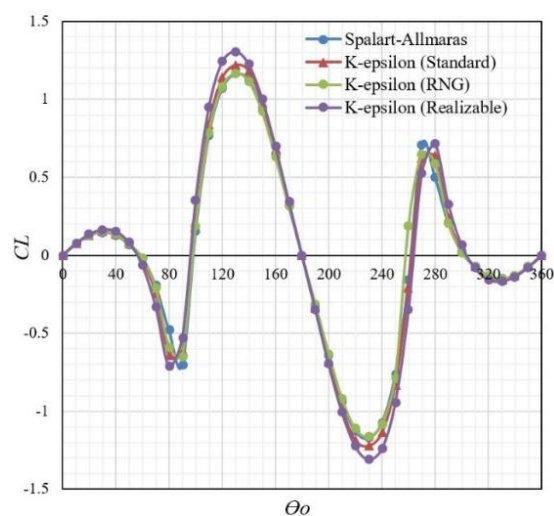
**Fig. 10.** Variation of pressure coefficient at the curved surface at  $Re = 2653.9$

Due to the lack of studies regarding employing the Spalart-Allmaras turbulent model in investigating the flow field characteristics around the semi-circular cylinder, we use three widespread turbulent models to verify the results obtained by the Spalart-Allmaras turbulent model and these models are  $k-\epsilon$  (standard),  $k-\epsilon$  (RNG), and  $k-\epsilon$  (Realizable). The comparative study deals with three parts: the first part gives a good agreement with the obtained results from the different turbulent

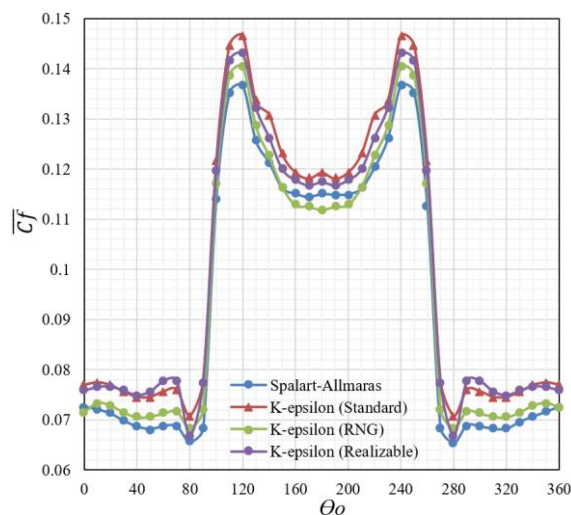
models; the Spalart-Allmaras has a moderate location among the curves of the remainder turbulent models without any contrast. The second part gives an excellent agreement in the obtained results from the different turbulent models, there is no variation among the curves. In addition, the third part gives a good agreement with the obtained results from the different turbulent models. Here, the first part deals with the drag coefficient (Figure 11), the second part deals with the lift coefficient (Figure 12), and the third part deals with the skin friction factor (Figure 13). These three dimensionless parameters are drawn with all values of the angles. It is visible from Figure 11, Figure 12 and Figure 13 (drawn with Reynolds number equal to 2653.9) that the comparative study satisfies the required target from the numerical study, it is confirmed that the use of various turbulent models does not affect the hydraulic parameters regardless of the angle values.



**Fig. 11.** Variation of drag coefficient with rotation angle using different turbulent models



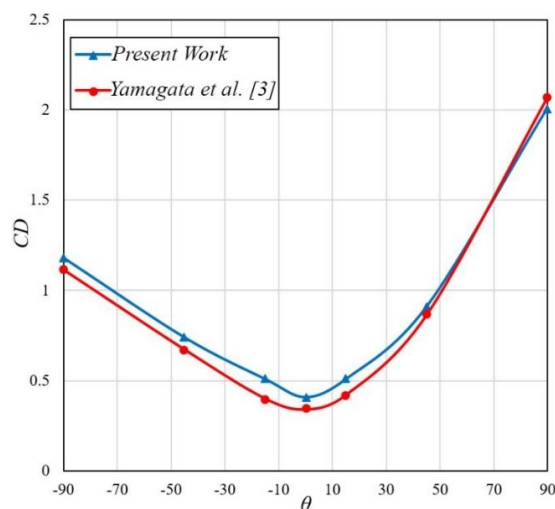
**Fig. 12.** Variation of lift coefficient with rotation angle using different turbulent models



**Fig. 13.** Variation of skin friction with rotation angle using different turbulent models

### 3.1 Comparative Study

Figure 14 illustrates the semi-circular cylinder drag coefficient for different attach angles at  $Re=6.7 \times 10^4$ . It is seen from the Figure 14 that both the previous study done by Yamagata *et al.*, [3] and the current study have the same trend in the relation between the drag coefficient and the attack angles without any variation, this point strengthens the current study and gives an invaluable indicator. It should be stated here that Yamagata *et al.*, [3] adopted constant surface area when evaluating the drag coefficient and for the sake of comparison, the same assumption is considered.



**Fig. 14.** Comparative study for the relation between the drag coefficient and rotation angle

## 4. Conclusions

The water flow past a semi-circular cylinder with various angles of attack, was examined using the Spalart-Allmaras turbulence model in ANSYS Fluent. The current paper focused on the flow velocity vector, velocity contours, and pressure contours in order to produce a good image about flow direction around the cylinder and how the velocity field will change owing to the variation in the value of angles. For example, based on the flow velocity contours, it is clear from contours at angle  $150^\circ, 160^\circ, 170^\circ$  and  $180^\circ$ , all the flow velocity magnitudes of the field are to somewhat identical and there is variation. In addition, the pressure field reflects how the pressure changes from positive to negative or from negative to positive and will reflect directly on the lift coefficient, while the flow velocity behavior will reflect directly on the drag coefficient and skin friction factor. The study adopted two different Reynolds numbers to express the impact of this number on the drag coefficient, lift coefficient, and skin friction factor. Reynolds number value has a direct effect on the drag coefficient and skin friction factor while in the case of lift coefficient the result shows there is no direct relation between the lift coefficient and Reynolds number. To ensure that the computed values of drag coefficient, lift coefficient, and skin friction factor using Spalart-Allmaras are suitable and reasonable. We use three different turbulent models to check the obtained results; moreover, the computed values by using the other turbulent models give results are somewhat very similar to results computed by using Spalart-Allmaras without any contrast in the results. The pressure coefficient values are based mainly on the flow separation along the wetted perimeter of the

semicircular cylinder. We advise further work analysis of the flow around the semicircular cylinder under the effect of different values of the Reynolds number.

## References

- [1] Lysenko, Dmitry A., Mark Donskov, and Ivar S. Ertesvåg. "Large-eddy simulations of the flow over a semi-circular cylinder at  $Re= 50000$ ." *Computers & Fluids* 228 (2021): 105054. <https://doi.org/10.1016/j.compfluid.2021.105054>
- [2] Isaev, Sergey, Paul Baranov, Igor Popov, Alexander Sudakov, Alexander Usachov, Sergey Guvernyuk, Alexei Sinyavin et al. "Numerical simulation and experiments on turbulent air flow around the semi-circular profile at zero angle of attack and moderate Reynolds number." *Computers & Fluids* 188 (2019): 1-17. <https://doi.org/10.1016/j.compfluid.2019.03.013>
- [3] Yamagata, Takayuki, Nozomi Saito, and Nobuyuki Fujisawa. "Aeolian tone from a semi-circular cylinder in a stream." *Journal of Flow Control, Measurement & Visualization* 4, no. 1 (2015): 30-37. <https://doi.org/10.4236/jfcmv.2016.41003>
- [4] Wornom, Stephen, Hilde Ouvrard, Maria Vittoria Salvetti, Bruno Koobus, and Alain Dervieux. "Variational multiscale large-eddy simulations of the flow past a circular cylinder: Reynolds number effects." *Computers & Fluids* 47, no. 1 (2011): 44-50. <https://doi.org/10.1016/j.compfluid.2011.02.011>
- [5] Tsutsui, Takayuki. "Flow around a cylindrical structure mounted in a plane turbulent boundary layer." *Journal of Wind Engineering and Industrial Aerodynamics* 104 (2012): 239-247. <https://doi.org/10.1016/j.jweia.2012.05.003>
- [6] Zhang, Chaofan, Stéphane Moreau, and Marlène Sanjosé. "Turbulent flow and noise sources on a circular cylinder in the critical regime." *AIP Advances* 9, no. 8 (2019). <https://doi.org/10.1063/1.5121544>
- [7] Yagmur, Sercan, Sercan Dogan, Muharrem Hilmi Aksoy, and Ilker Goktepel. "Turbulence modeling approaches on unsteady flow structures around a semi-circular cylinder." *Ocean Engineering* 200 (2020): 107051. <https://doi.org/10.1016/j.oceaneng.2020.107051>
- [8] Barratt, Dylan, Jaehyoung Lee, Michael D. Atkins, Seung Jin Song, and Tongbeum Kim. "The kinematics of boundary layer transition on a long circular cylinder impinged by a fully turbulent round jet." *Experimental Thermal and Fluid Science* 99 (2018): 149-157. <https://doi.org/10.1016/j.expthermflusci.2018.07.038>
- [9] Pereira, Filipe S., Luís Eça, Guilherme Vaz, and Sharath S. Girimaji. "On the simulation of the flow around a circular cylinder at  $Re= 140,000$ ." *International Journal of Heat and Fluid Flow* 76 (2019): 40-56. <https://doi.org/10.1016/j.ijheatfluidflow.2019.01.007>
- [10] Salaheldin, Tarek M., Jasim Imran, and M. Hanif Chaudhry. "Numerical modeling of three-dimensional flow field around circular piers." *Journal of Hydraulic Engineering* 130, no. 2 (2004): 91-100. [https://doi.org/10.1061/\(ASCE\)0733-9429\(2004\)130:2\(91\)](https://doi.org/10.1061/(ASCE)0733-9429(2004)130:2(91))
- [11] Behrouzi, Zahra, Hossein Hamidifar, and Mohammad Ali Zomorodian. "Numerical simulation of flow velocity around single and twin bridge piers with different arrangements using the Fluent model." *Amirkabir Journal of Civil Engineering* 53, no. 9 (2021): 857-860.
- [12] Mammam, Mohamed, and Azeddine Soudani. "Numerical study of external turbulent flow." *Journal of Renewable Energies* 15, no. 1 (2012): 155-164. <https://doi.org/10.54966/jreen.v15i1.308>
- [13] Sowoud, K. M., A. A. Al-Filfily, and B. H. Abed. "Numerical investigation of 2D turbulent flow past a circular cylinder at lower subcritical Reynolds number." In *IOP Conference Series: Materials Science and Engineering*, vol. 881, no. 1, p. 012160. IOP Publishing, 2020. <https://doi.org/10.1088/1757-899X/881/1/012160>
- [14] Catalano, Pietro, Meng Wang, Gianluca Iaccarino, and Parviz Moin. "Numerical simulation of the flow around a circular cylinder at high Reynolds numbers." In *Engineering Turbulence Modelling and Experiments* 5, pp. 657-665. Elsevier Science Ltd, 2002. <https://doi.org/10.1016/B978-008044114-6/50063-6>
- [15] Alonzo-García, A., C. del C. Gutiérrez-Torres, and Jose Alfredo Jimenez-Bernal. "Large eddy simulation of the subcritical flow over a U-grooved circular cylinder." *Advances in Mechanical Engineering* 6 (2014): 418398. <https://doi.org/10.1155/2014/418398>
- [16] Singha, Sintu, and K. P. Sinhamahapatra. "Flow past a circular cylinder between parallel walls at low Reynolds numbers." *Ocean Engineering* 37, no. 8-9 (2010): 757-769. <https://doi.org/10.1016/j.oceaneng.2010.02.012>
- [17] Qasim, Rafi M., and Tahseen Ali Jabbar. "An Analytic Study of the Effect of a Vane on the Hydraulic Field around a Cylinder." *INCAS Bulletin* 13, no. 3 (2021): 123-139. <https://doi.org/10.13111/2066-8201.2021.13.3.11>
- [18] Qasim, Rafi M., Tahseen A. Jabbar, and Safaa H. Faisal. "Effect of the curved vane on the hydraulic response of the bridge pier." *Ocean Systems Engineering* 12, no. 3 (2022): 335-358.
- [19] Qasim, Rafi Mohammed, Safaa Hameed Faisal, and Tahseen Ali Jabbar. "Impact of T-splitter on the laminar flow field around cylinder pier." *Advances in Science and Technology. Research Journal* 16, no. 5 (2022). <https://doi.org/10.12913/22998624/154795>

- [20] Qasim, Rafi Mohammed, Tahseen Ali Jabbar, and Safaa Hameed Faisal. "Simulation of laminar flow passing through a T-splitter plate and bridge pier." *Scientific Review Engineering and Environmental Sciences* 32, no. 2 (2023): 135-154. <https://doi.org/10.22630/srees.4548>
- [21] Jabbar, Tahseen Ali, Rafi Mohammed Qasim, and Safaa Hameed Faisal. "Effect of T-shape splitter on the hydraulic response of the bridge pier." *UPB Scientific Bulletin, Series D* 84, no. 4 (2022): 263-280.
- [22] Jabbar, Tahseen Ali, Rafi M. Qasim, and Bassam A. Mohammed. "The Vane Angle Influence on the Flow Pattern around a Circular Pier." *U. Porto Journal of Engineering* 8, no. 6 (2022): 189-209. [https://doi.org/10.24840/2183-6493\\_008.006\\_0014](https://doi.org/10.24840/2183-6493_008.006_0014)
- [23] Sumer, B. Mutlu. *Hydrodynamics around cylindrical structures*. Vol. 26. World Scientific, 2006. <https://doi.org/10.1142/6248>
- [24] Spalart, Philippe, and Steven Allmaras. "A one-equation turbulence model for aerodynamic flows." In *30th Aerospace Sciences Meeting and Exhibit*, p. 439. 1992. <https://doi.org/10.2514/6.1992-439>
- [25] Launder, Brian Edward, and Dudley Brian Spalding. "The numerical computation of turbulent flows." *Computer Methods in Applied Mechanics and Engineering* 3, no. 2 (1974): 269-289. [https://doi.org/10.1016/0045-7825\(74\)90029-2](https://doi.org/10.1016/0045-7825(74)90029-2)
- [26] El Maani, Rabii, Soufiane Elouardi, Bouchaib Radi, and Abdelkhalek El Hami. "Study of the turbulence models over an aircraft wing." *Incert Fiabilité Des Systèmes Multiphysiques* 2, no. 2 (2018): 1-11. <https://doi.org/10.21494/ISTE.OP.2018.0306>
- [27] Douvi, C. Eleni, I. Athanasios Tsavalos, and P. Dionissios Margaritis. "Evaluation of the turbulence models for the simulation of the flow over a National Advisory Committee for Aeronautics (NACA) 0012 airfoil." *Journal of Mechanical Engineering Research* 4, no. 3 (2012): 100-111. <https://doi.org/10.5897/JMER11.074>